Group and phase delay sensing for cophasing large optical arrays

D. Mourard, W. Dali Ali, A. Meilland, Nassima Tarmoul, F. Patru, J. M. Clausse, Pascal Girard, F. Henault, A. Marcotto, N. Mauclert

To cite this version:

D. Mourard, W. Dali Ali, A. Meilland, Nassima Tarmoul, F. Patru, et al.. Group and phase delay sensing for cophasing large optical arrays. Monthly Notices of the Royal Astronomical Society, 2014, 445 (2), pp.2082-2092. 10.1093/mnras/stu1790 . hal-01139448

HAL Id: hal-01139448
https://hal.science/hal-01139448

Submitted on 9 Dec 2020

Monthly Notices
of the
ROYAL ASTRONOMICAL SOCIETY

MNRAS **445,** 2082–2092 (2014) doi:10.1093/mnras/stu1790

Group and phase delay sensing for cophasing large optical arrays

D. Mourard,[1]⋆ W. Dali Ali,[1] A. Meilland,[1] N. Tarmoul,[2] F. Patru,[3] J. M. Clausse,[1] P. Girard,[1] F. Hénault,[4] A. Marcotto[1] and N. Mauclert[1]

[1]*Laboratoire J.L. Lagrange, UNS/OCA/CNRS – CS64209, F-06304 Nice cedex, France*
[2]*LATMOS, 11 Bd D'Alembert, F-78280 Guyancourt, France*
[3]*Osservatorio Astrofisico di Arcetri, 5 Largo Enrico Fermi, I-50125, Firenze, Italy*
[4]*IPAG, 414 rue de la piscine, F-38400 Saint-Martin d'Hères, France*

Accepted 2014 September 1. Received 2014 August 28; in original form 2014 May 4

ABSTRACT

The next generation of optical interferometers will provide high-resolution imaging of celestial objects by using either the aperture synthesis technique or the direct imaging principle. To determine the technical requirements, we have developed an interferometric test bench, called SIRIUS. To preserve the quality of the image, fast corrections of the optical path differences within a fraction of a wavelength have to be applied: this is the cophasing of the array, whereas making it coherent aims at stabilizing the optical path differences within a fraction of the coherence length. In the SIRIUS test bench, coherence and cophasing are achieved by fibred delay lines. Air delay lines are also used for the raw delay equalization. We present an original implementation of a piston sensor, called chromatic phase diversity, which is adaptable to any interferometer, whatever the configuration of the entrance pupil and the number of sub-pupils and whatever the interferometric combiner. Our method is based on the dispersed fringes principle and uses a derived version of the dispersed speckles method. The numerical simulation shows the performance of the method in terms of cophasing, accuracy and limiting magnitude. Experimental tests have been carried out both with optical turbulence and without. They show good results in both cases, despite some instrument-related limitations that can be eliminated. We show that our method is able to handle an amplitude of correction of $\pm 11(\lambda/2)$ with an accuracy of $\sim\lambda/30$ over many minutes.

Key words: instrumentation: interferometers – techniques: high angular resolution – Telescopes.

1 INTRODUCTION

Coherently combining the signals from several telescopes is used to achieve the high angular resolution provided by the large dimension of an interferometer. The critical point is coherently combining the beams within a fraction of a wavelength (see for instance Patru et al. 2010). The optical path differences (OPDs), the atmosphere perturbations and the instrumental instabilities should be measured accurately and in real time, and then compensated by optical delay lines (DLs). This is crucial for long exposures without blurring the high angular resolution signals and to improve the sensitivity or the signal to noise ratio (SNR).

Active cophasing was first implemented on the Mark III interferometer (Shao et al. 1988) and its successors (NPOI, PTI, Keck Interferometer) (Colavita et al. 1998). It was then applied to the Very Large Telescope Interferometer (VLTI) (Glindemann et al. 2004) and CHARA interferometer (ten Brummelaar et al. 2005). In the most common implementation, two beams are combined pairwise while a mirror is stepped at quarter-wavelength intervals resulting in four measurements (A,B,C,D) representing four different fringe phases. Known as the ABCD method, it mathematically represents a discrete Fourier transform of the signal. Coherence is achieved by active fringe scanning (FS) for FINITO (Gai et al. 2004) on the VLTI and on IOTA (Morel et al. 2000) or by group delay sensing like on GI2T, NPOI, PTI, Keck, CHARA and VLTI. Thanks to the spectral dispersion, larger delays ($>\lambda$) can be measured. The most used method is the dispersed fringes (DF) method introduced by Koechlin et al. (1996), where the fringes associated with each baseline are dispersed in a broad-band spectral channel. This technique is well adapted to a pairwise combination but complex linear reconfiguration of the pupils is also possible, as demonstrated by Monnier et al. (2008) and Mozurkewich & Traore (2010). However, a large number of telescopes leads to a complex optical set-up and a very large number of pixels to avoid redundancy. Combining spectral dispersion with a two-dimensional (2D) pupil configuration

---

⋆ E-mail: denis.mourard@oca.eu

Published by Oxford University Press on behalf of the Royal Astronomical Society

has been proposed with the dispersed speckle (DS) method (Martinache 2004; Borkowski et al. 2005). This method, which consists in generating a cube of spectrally dispersed images, can be applied to an arbitrary number of apertures in any geometrical configuration. Nevertheless, this method needs a long processing time and any real-time tracking appears impossible.

The implementation of phase and group delay sensing that we propose here, which is called the chromatic phase diversity (CPD) method, can deal with the future need for large interferometers and with processing performance with regard to time. It is inspired by the DS method and is based on using a small number of spectral channels.

In this paper, we detail the CPD method in Sections 2 and 3. We then characterize the main parameters of the method through different relevant numerical examples in Section 4. The optical implementation of the piston sensor on the SIRIUS test bench and the main limitations are presented in Section 5. In Section 6, we discuss the performance with optical turbulence and in Section 7 we compare the CPD method with other implementations of group and phase delay sensing. Finally, a conclusion and future possible developments are given in Section 8.

2 GENERAL PRINCIPLE OF THE CPD METHOD

If we consider the future large arrays, the cophasing system should be easy to implement and efficient, i.e. fast, sensitive and accurate. It should also be robust to fast jumps in OPD, either due to system misbehaviour (the phase jump effect) or to atmospheric turbulence. It is designed to reach an OPD range of about 10–20λ, close to standard atmospheric jitter. The optical design is also intended to make, with the minimum number of pixels, the best possible use of dedicated spectral bands in terms of sensitivity. The CPD method allows simultaneous control of coherence and cophasing for enhanced robustness. The principle of the CPD algorithm is based on the classical group delay and phase delay principles but the originality is in its optical implementation, which opens up interesting perspectives.

Regarding the optical design of the spectroscopic sensor, we have considered different solutions: a field spectrograph, a multibandpass chromator and a simple set of complementary dichroics. This last solution has been finally adopted, considering that three different spectral bands will be optimal in terms of sensing performance and in terms of actual optical implementation. Thus, three images at three different wavelengths are recorded simultaneously by the sensor device. The Fourier transform of these images gives the phase delays corresponding to each baseline at each wavelength. For one baseline and one wavelength, the measured phase can be used to estimate the corresponding piston but the estimation is unambiguous only if the piston is smaller than $\pm\lambda/2$. Using three wavelengths means this limit can be increased up to almost the coherence length. All the associated OPDs can then be extracted over a large capture range (CR) and can be corrected (Gonsalves 1982; Houairi & Cassaing 2009). Although the piston determination is based on the phase only, we will see later that control of the amplitude is also important for improving the reliability of the phase measurement and thus the overall robustness of the sensor.

The optical design of the interferometric combiner takes advantage of the hypertelescope concept based on a densified pupil multiaxial combining scheme (Labeyrie 1996) and providing an optimal direct imaging capability at the combined focus of the interferometer. We assume that the densification factor is chosen so that the optical transfer function (OTF) does not contain overlap areas, which corresponds in our case to a factor equal to 0.4. Although we consider an homothetic mapping of the entrance pupil for the recombining scheme of the cophasing sensor (see Fig. 1), it does not need to match the entrance configuration, as is the case for a hypertelescope. Whatever the entrance configuration of the interferometer (redundant or not) and whatever the scientific recombiner (aperture synthesis with a classical combiner or direct imaging with a hypertelescope), the sub-pupils can be rearranged at the entrance of the piston sensor with the required configuration. For a redundant pupil configuration of the interferometric array, a non-redundant pupil configuration could feed the entrance of the piston sensor. Note that the problem of redundancy of the array has been addressed in previous papers (see for instance Martinache 2004 and Patru et al. 2009). A multi-axial optical scheme is easy to implement and does not dramatically change the number of sub-pupils. Finally, the optical scheme shown here is well suited to cophase any kind of future large interferometer (Patru et al. 2007; Tarmoul, Mourard & Hénault 2008).

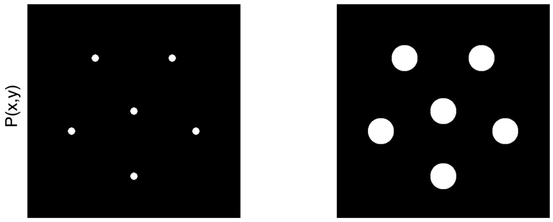

Figure 1. Entrance (left) and output (right) pupil planes of the piston sensor. For SIRIUS, we use a configuration with five apertures of 2.7 mm diameter separated with a maximum baseline of 49 mm plus a sixth aperture at the geometrical centre of the figure. The densified beams have a 9.8 mm diameter.

In the following, we assume that all sub-apertures of the array are equipped with adaptive optics and spatial filtering through single-mode fibres (Patru et al. 2007). This kind of fibred combiner is currently implemented on the SIRIUS test bench (Patru et al. 2008; Tarmoul et al. 2010a) located at the Observatoire de la Côte d'Azur (France). First, the flexibility of the fibres enables one to recreate a non-redundant pupil configuration with concentric circles to feed the piston sensor with the most compact chromatic images. Second, the spatial filtering properties of the fibres average out the residual piston within each sub-pupil so that the cophasing will just have to deal with residual differential pistons between the sub-pupils (Patru et al. 2007, 2008; Lardière, Martinache & Patru 2007). Third, spatial filtering improves the robustness of the piston sensor by minimizing the problem of phase jumps. A phase jump occurs with large arrays (like KECK, CHARA and VLTI) using apertures much larger than the Fried parameter r_0, for which diffraction effects can induce phase anomalies between the real phase and the measured phase. These effects can induce large and sudden jumps in the phase. Thanks to spatial filtering, a single instantaneous phase value is transmitted in each sub-pupil, so that the phase jumps are less frequent in a filtered combiner (Buscher et al. 2008). Finally, single-mode spatial filtering should improve the accuracy of the estimated residual pistons and should reduce the phase jump effects due to the system.

The CPD method is a new implementation of the group delay and phase delay principles. The optical scheme for the piston sensor has been revisited and is mainly composed of:

(i) a spectrograph, providing three resolved images in three different spectral bands (with a set of complementary dichroics),

(ii) a multi-axial beam combiner (by combining several beams in a 2D pupil plane directly in the focal plane),

(iii) pupil densifier (by increasing the relative size of the sub-pupils compared with the size of the baselines),

(iv) a sub-pupil single-mode filter (by using single-mode fibres on each of the sub-pupils),

(v) a fibred delay-line (by stretching the fibres).

More details are given in Section 5 and in Figs 8 and 9.

3 MATHEMATICAL DESCRIPTION OF THE METHOD

As with any group delay implementation using spectral dispersion, the method takes advantage of the relation between the differential piston value and the phase measured at a few discrete wavelengths. If we consider the baseline (u, v), the differential phase value $\varphi(u, v)$ depends on both the piston value $\delta(u, v)$ and the observation wavelength λ as follows:

$$\varphi(u, v) = \frac{2\pi\delta(u, v)}{\lambda}. \tag{1}$$

However, the estimation of a phase is always done with a $2k\pi$ uncertainty, k being a relative integer. Thus, the sought piston $\delta(u, v)$ can be determined by resolving:

$$\delta(u, v) = \frac{\lambda\varphi(u, v)}{2\pi} \pm k\lambda. \tag{2}$$

It should be noted that the parameter k leads to a problematic ambiguity for the piston. To resolve this ambiguity, and as in the DS method (Borkowski et al. 2005), the idea is to record several images at different wavelengths. The proposed implementation is based on three wavelengths and is an adaptation of the algorithm developed by Lofdahl & Eriksson (2001), so that real-time cophasing can be achieved.

We start our mathematical description by introducing the entrance pupil plane of the interferometer to be cophased. For simplicity, we assume that the sub-apertures are circular, have the same diameters and are in the configuration shown in Fig. 1. The chosen configuration gives an optimal densification factor (see Fig. 2) without introducing overlap areas in the OTF (see Fig. 3). We can define the complex amplitude $P(u, v)$ of the wave in the pupil plane (u, v) as:

$$P(u, v) = |P(u, v)|e^{2i\pi\delta(u,v)/\lambda} \tag{3}$$

where $|P(u, v)|$ is the amplitude of $P(u, v)$, and $\delta(u, v)$ represents the piston function in the (u, v) plane and λ the wavelength.

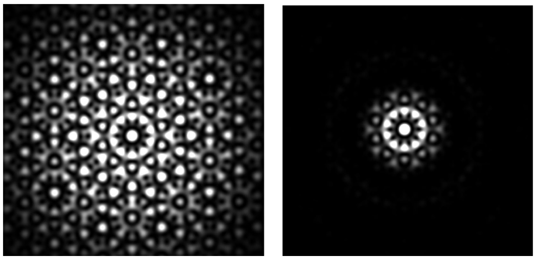

Figure 2. PSF obtained in entrance plane (left) and in the densified output plane (right). Pupils are densified 3.6 times, which corresponds to 40 per cent of the value allowed with this array configuration.

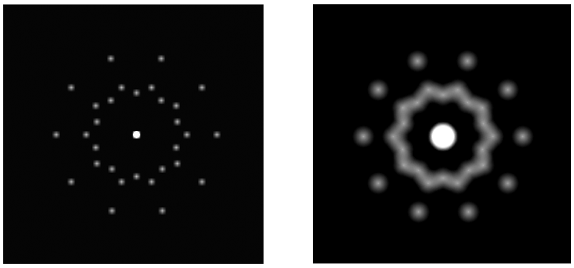

Figure 3. Optical transfer function OTF(u, v) of the image in Fig. 2: each baseline is identified according to the configuration illustrated in Fig. 1. OTF(u, v) corresponding to the images obtained at the entrance plane (left) and at the densified pupil plane (right).

We consider the case of a point-like source and thus the image given by the instrument is simply the point spread function (PSF). It is defined in the image plane (x, y):

$$PSF(x, y) = |FT[P(u, v)]|^2 \tag{4}$$

where FT represents the Fourier transform operation. Fig. 2 shows that the PSF in the densified pupil plane concentrates most of the energy in the central peak, whereas in the FIZEAU pupil plane the energy is spread over a larger zone. For the SIRIUS experiment, we tested the method on a densified pupil.

In the first step of the proposed piston sensor, one has to record three images at three wavelengths: λ_1, λ_2 and λ_3. For each given λ_n $(n = 1, 2 \text{ or } 3)$, the image intensity can be expressed as:

$$I(x, y)_{\lambda_n} = PSF(x, y)_{\lambda_n}. \tag{5}$$

Taking the inverse 2D Fourier transform of these images gives three complex OTFs:

$$\mathrm{OTF}(u, v)_{\lambda_n} = \mathrm{FT}^{-1}[I(x, y)_{\lambda_n}]. \tag{6}$$

Fig. 3 shows the modulus of the OTF: each baseline is identified with its associated peak. We note that for a densified pupil, fringe peaks overlap as the densification rate increases. To prevent the peaks overlapping (Fig. 4), we fixed the densification rate at 40 per cent of the maximum possible value with this configuration. Note that in our case, the entrance pupil plane is slightly diluted. In other actual cases, the pupil configurations could be more diluted and thus the method can be used with a larger densification ratio to improve the sensitivity.

The next step of the method consists in extracting the phase value of the OTF for each baseline (u, v):

$$\varphi(u, v)_{\lambda_n} = \arctan\left(\frac{Im[\mathrm{OTF}(u, v)_{\lambda_n}]}{Re[\mathrm{OTF}(u, v)_{\lambda_n}]}\right) \tag{7}$$

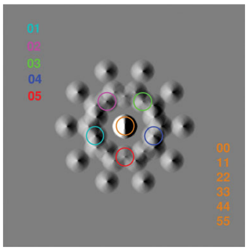

Figure 4. Peaks marked with circles are used in our method to estimate the pistons. They correspond to the OPDs between the central beam (0) and the five beams (1 to 5). With 40 per cent of the densification rate and the chosen entrance configuration, the peaks of interest do not overlap.

with $\varphi(u, v)_{\lambda_n} \in [-\pi, +\pi]$ by taking into account the signs of the imaginary and real parts.

If we consider an interferometer with N_T sub-pupils, we need to extract $(N_T - 1)$ differential phase values (from the $N_T(N_T - 1)/2$ values available) of the $\mathrm{OTF}(u, v)_{\lambda_n}$ at each λ_n.

The $(N_T - 1)$ chosen baselines correspond to the pairs of pupils made by each peripheral sub-pupil and the central one considered as the reference one.

For a specific baseline (u, v) and one of the three wavelengths, an infinity of solutions (modulo the chosen wavelength) exists for the determination of $\delta(u, v)$ according to equation (2). If one takes into account the three wavelengths, then an infinity of solutions still exists but there is a much larger periodicity, which is called the synthetic wavelength or the *capture range* (CR) (Lofdahl & Eriksson 2001). So, the same piston $\delta(u, v)$ is present in the three sets of solutions. It corresponds exactly to the first overlap of these sets.

3.1 Determination of the capture range

In this section, we give the procedure to calculate the maximum CR in the general case (Lofdahl & Eriksson 2001). We do not consider here external limitations such as low visibility or fast turbulence. This method allows the determination of the CR whatever the number of spectral bands used, their central wavelength and their spectral width. For this calculation, we consider a null piston on a given baseline. For the monochromatic channels the overlapping zone is given by:

$$k_1\lambda_1 = k_2\lambda_2 = k_3\lambda_3. \tag{8}$$

Since we use different wavelengths, the order of overlapping $k_{1,\,2,\,3}$ are not only different but >1. This means that the CR is necessarily larger than each wavelength considered individually. In practice, the channels are given by spectral filters with non-zero spectral bandwidth ($\Delta\lambda_i = 2E_i$). Then for each pair of wavelengths, the zone of the overlapping sets can be determined such as:

$$|k_i\lambda_i - k_j\lambda_j| < E_i + E_j. \tag{9}$$

For solving this, we need to find the smallest integers k_i and k_j satisfying equation (9) for two wavelengths (λ_1 and λ_2), with $\lambda_1 > \lambda_2$. Using the theory of the regular continued fraction, the ratio λ_1/λ_2 can be expressed as a sequence of rational fractions that approaches the exact value: $\{a_1/b_1,\ a_2/b_2,\ \ldots,\ a_l/b_l\}$ with $a_{l+1} > a_l$ and $b_{l+1} > b_l$. These fractions are called the approximates of the quantity λ_1/λ_2. The CR is given by the largest of the two numbers $\{k_1\lambda_1 - E_1,\ k_2\lambda_2 - E_2\}$, where $k_2/k_1 = a_l/b_l$ is the first approximate satisfying:

$$b_l < \lambda_2/(E_1 + E_2) < b_{l+1}, \tag{10}$$

where b_l and b_{l+1} are the denominators of two consecutive approximates of λ_1/λ_2. Consequently, the CR will be extended to $\sim k_1\lambda_1$. To get a large CR, the ratio of two wavelengths should be different from any rational fraction with small denominator.

The CR acts as the synthetic wavelength λ_{12} of the system $(\lambda_1,\ \lambda_2)$. It means that a unique solution could be found in the interval $[-\lambda_{12}/2\ \lambda_{12}/2]$. Using a third wavelength λ_3 with a spectral width $2E_3$, the same method can be applied and it provides a new CR for the system $(\lambda_{12},\ \lambda_3)$, which will be the largest value of $\{k_3\lambda_3 - E_3,\ k_{12}\lambda_{12} - (E_1 + E_2)\}$. In this case, the approximate $k_3/k_{12} = a'_l/b'_l$ satisfies:

$$b'_l < \lambda_3/(E_1 + E_2 + E_3) < b'_{l+1}. \tag{11}$$

Table 1. Configuration of the three spectral bands.

λ_i (nm)	552	600	665
$\Delta\lambda_i = 2E_i$ (nm)	40	60	60

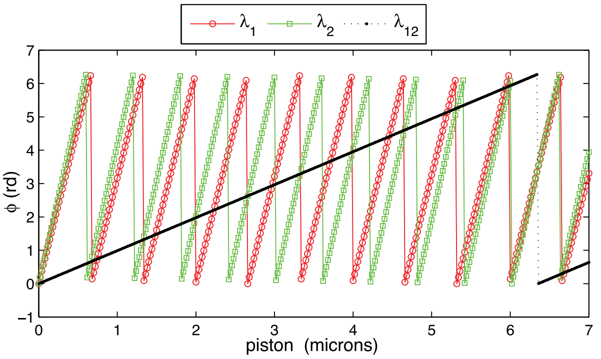

Figure 5. Capture range appears as a synthetic wavelength (λ_{12}) composed of λ_1 and λ_2. In this case the CR is 11 times the smallest wavelength.

By choosing an adequate λ_3, the new CR is $\sim k_{12}$ times the one given by two wavelengths. For our experiment, we took a set of three wavelengths and associated bandwidths, as given in Table 1.

The only drawback of using three spectral channels is the fact that more pixels are needed. This must be considered carefully with respect to the constraints on the detector read-out noise (RON) such as in the infrared. As shown in Fig. 5, according to the method explained below, the resulting CR from this set is 6 μm with two wavelengths. Indeed, the first approximate of the quantity λ_1/λ_2 that satisfies equation (10) is 11/10, thus the CR is $\sim 11\lambda_2$ or $\sim 10\lambda_1$. When using the three wavelengths the resulting CR is 34 μm. This value is clearly adapted to the experiment since we almost cover the whole coherence length of the spectral channels (from 6–8 μm).

3.2 Determination of the unambiguous solution

As shown by equation (1), the differential phase $\varphi(u, v)$ is known modulo 2π: the issue is to determine the correct value and solve the ambiguity. The corresponding piston $\delta(u, v)$ is determined in two steps as follows: first we evaluate sets of the potential pistons corresponding to two wavelengths, δ_{λ_1} and δ_{λ_2}, as $\delta_1 \pm k_1\lambda_1$ and $\delta_2 \pm k_2\lambda_2$ with the $k_{1,\,2}$ integers varying from 0 to N. The solution will correspond to the first overlap of the two sets.

$$|\delta_{\lambda_1} - \delta_{\lambda_2}| \leq \epsilon_{12} \tag{12}$$

where ϵ_{12} is the precision for the solution determination. This solution is unique in the CR given by the pair of these wavelengths, which we denote as λ_{12}. However, we know that this solution will be repeated modulo λ_{12}. Using the third wavelength λ_3, we evaluate the corresponding potential pistons as $\delta_3 \pm k_3\lambda_3$ and that given by the synthetic wavelength λ_{12} as $\delta_{12} \pm k_{12}\lambda_{12}$. The final solution will be given by the first overlap of these two last sets:

$$|\delta_{\lambda_{12}} - \delta_{\lambda_3}| \leq \epsilon_{123}, \tag{13}$$

where ϵ_{123} is the precision for the final solution determination. This solution is indeed unique in the new CR which is given by the three wavelengths.

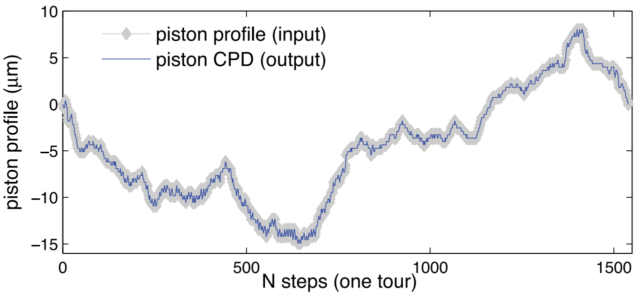

Figure 6. Recovering the piston values introduced on the sub-pupils, by using the method with three wavelengths. The input piston profile used in this simulation corresponds to the experimental profile measured at Paranal with FINITO open-loop device.

4 TESTS OF THE METHOD THROUGH NUMERICAL SIMULATIONS

The performance was first studied by numerical simulation. The first part of the simulation checks the performance of the algorithm regarding the phase fluctuations and the phase noise effect. In the second part, other limitations are introduced: shot noise, background noise, dark current and RON. The star magnitude is introduced for sensitivity analysis. A detailed description of the simulation is given in a dedicated paper (Tarmoul et al. 2010b). Here we only highlight the performance of the algorithm versus the object magnitude. For the purpose of the simulation as for the actual implementation on the SIRIUS test bench, the choices of the spectral bands have been driven by two main considerations: (1) a wide spectral band is dedicated to the cophasing sensor and the whole band has to be used for sensitivity concerns, (2) the CR should be maximized so that it reaches at least a value larger than the standard deviation of the atmospheric piston (±10 µm) and close to the smallest coherence lengths of the different bands.

4.1 Validation of the algorithm

The numerical simulations were performed using the IDL language to validate the cophasing method. We simulate the array configuration of SIRIUS with six densified sub-pupils as shown in Fig. 1. Random pistons are introduced on the sub-pupils of the entrance plane. The program calculates the corresponding images at the focus of the instrument for the three wavelengths. After applying a Fourier transform to these images, we recover the piston information for each baseline by using the algorithm described in Section 3.

As shown in Fig. 6, pistons calculated using three wavelengths match exactly the values introduced on the entrance sub-pupil. These input values of the piston correspond to a piston profile extracted from FINITO data in open-loop mode (Lebouquin 2012).

4.2 Performance reached in terms of magnitude

Using the numerical model, we estimated the limiting magnitude on the sky in both coherence (group delay) and cophasing (phase delay) modes and combining four or six telescopes of the VLTI (Tarmoul et al. 2010b). We assumed non-redundant configurations of the exit pupils when coupling four auxiliary telescopes (ATs) in a multi-axial recombination mode. We performed these simulations using the parameters specified for the second generation of VLTI fringe tracker (second GFT) by ESO (Lebouquin 2010) and summarized in Table 2 for the two modes of correction: cophasing and coherence.

Central wavelengths chosen in the K band are 2, 2.2 and 2.4 µm with spectral widths of 0.2 µm. This gives a CR of 38 µm, which is larger than the coherence length $\lambda^2/\Delta\lambda = 24\mu$, so this means that the cophasing could be done along all the coherence length. The integration time is set to 0.5 ms in phase-delay mode and 5 ms in group-delay mode according to the actual atmospheric conditions at Paranal where the coherence time of turbulence is typically ∼5 ms (Dali Ali et al. 2010). Note also that these values are coherent with the specifications given in Table 2. However, we also consider an improved mode with longer exposure times (10 ms for phase delay and 25 ms for group delay), permitted when seeing conditions are excellent. Fig. 7 (top) shows the achieved piston measurement accuracy as a function of the magnitude of the target star for the two modes (phase delay and group delay). We define the success ratio as the percentage of time where the OPD is correctly determined. One should note that the principle of the method sets the piston resolution to 10 nm, which explains why with bright stars this value does not improve. The limiting magnitude is defined for a success ratio of 50 per cent. We note that the proposed method is thus successful until magnitude 7.5 for usual atmospheric conditions. In good conditions of turbulence, we can gain 2 mag. At this stage, the method has the same performance as the ABCD method also proposed for second GFT studies.

In these calculations, we considered the RON (10 electrons/pixel) of the existing detectors. It appears that the magnitude limit can be improved if we use a detector with less RON. As shown in Fig. 7 (bottom), we gain 1.5 mag for RON =1.5 electrons/pixel. This is an encouraging point thanks to the recent progress in this domain.

The combination of six telescopes was also studied. The results show that adding two Auxilliary Telescopes (ATs) does not improve the performance. But if we add two Unit Telescopes (UTs) instead of the two ATs this will gain almost 2 mag as demonstrated by Tarmoul et al. (2010b).

Indeed, adding two telescopes will increase the total surface and the number of photons. But, this will also decrease the minimum baseline of the array (B_{min}). This leads to an increase in the number of pixels N_{pixel} requested on the detector for the useful image. So adding two UTs instead of two ATs, does not change B_{min} (N_{pixel}), but increases the total surface. The number of photons is larger and the SNR is better.

Table 2. Specifications of the second-generation ESO fringe tracker for the two considered modes: cophasing and coherence. The table gives the acceptable noise level on the residual OPD, the frequency of correction, the acceptable time delay between the measurement and the correction, the OPD resolution and linearity.

	Phase delay	Group delay
Noise (RMS)	≤100 nm	≤ 800 nm
Rate	≥2 kHz	≥200 Hz
Pure delay	≤600 μs	≤10 ms
OPD resolution	≤1 nm	–
Linearity	≥10 per cent over a range of ±1050 nm	≥20 per cent over a range of ±6 µm

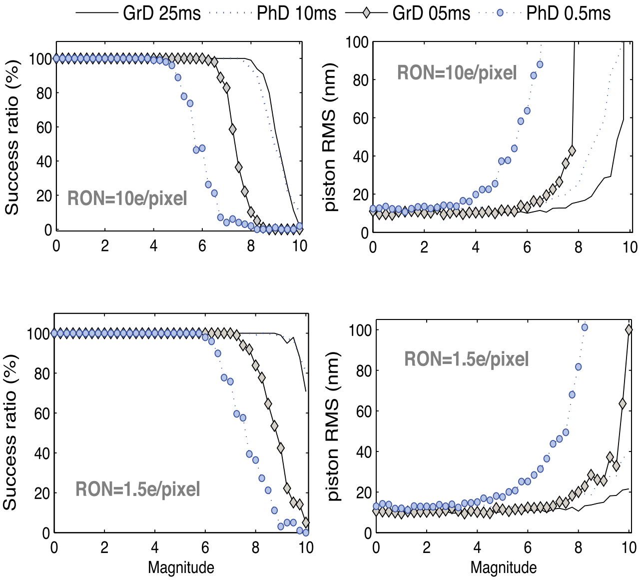

Figure 7. Results obtained in group delay mode (solid/solid+diamond) and phase delay mode (dot/dot+circle) when combining four ATs. Success ratios (left) and piston measurement errors (right) are expressed as a function of the magnitude of the guide star. Top: Values obtained for the existing detectors with RON = 10 electrons/pixel. Bottom: Those obtained with RON = 1.5 electrons/pixel.

5 APPLICATION ON THE SIRIUS TEST BENCH

5.1 Description of the optical set-up

The first version of the SIRIUS test bench (Patru et al. 2008) was designed to characterize the hypertelescope concept according to the VLTI configuration (scale 1/3000) and with respect to the direct imaging capabilities. The current test bench is now equipped with a cophasing device aiming at validating the proposed method. The main requirement was to be easily adaptable to any number of telescopes, as will be required for the future large arrays. Moreover, this method was specified to be easily implemented and compact by using fibred DLs. The block diagram of the test bench is shown in Fig. 8.

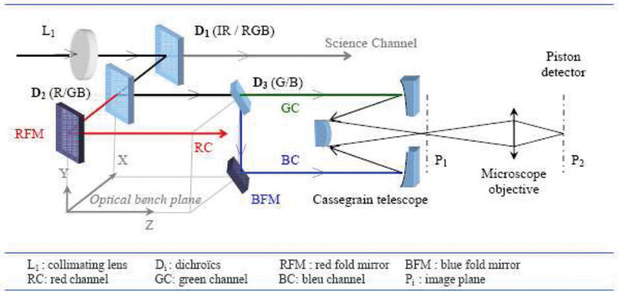

Figure 9. Optical set-up of the sensor part. The beam from dichroic D1 (visible part, RGB) is separated into three spectral channels (RC, GC and BC) using two dichroics (D2 and D3) and two mirrors (RFM and BFM), all positioned in a three-dimensional configuration (x, y, z). The monochromatic beams are imaged with a Cassegrain telescope and converged (via a microscope objective) to three separate locations of the same sensor plane.

The array configuration is composed of six sub-pupils (Tarmoul et al. 2010a) arranged as in Fig. 1. Each transmitted beam is injected into a fibred DL with an achromatic lens. We use a white coherent light source with a large spectrum (400–1100 nm). As shown in Fig. 9, the light is separated via a dichroic lens into two parts: the infrared part (>700 nm) is directed towards the science camera, whereas the visible part (500–700 nm) is divided into three monochromatic channels using two other dichroics and directed to the piston sensor system. The algorithm is applied to the recorded images to extract the pistons. The piston are then converted into commands of the fibred DLs to achieve a real-time closed loop.

5.2 Results obtained with the SIRIUS test bench

In this section, we present the performance of the method as well as the main limitations with different instrumental constraints. Because we used an old computer, we encountered some issues with the calculation time for applying the algorithm in exact real time. The processing time should indeed be smaller than the piston time evolution. Actually, with only the internal low-frequency turbulence and drift in the lab, the execution time of the algorithm is

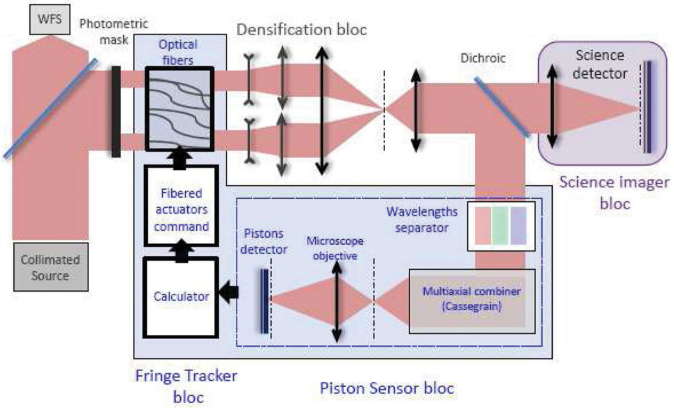

Figure 8. SIRIUS configuration: a collimated beam comes from a coherent white light source towards a beam splitter. The transmitted part is directed to the wavefront sensor (WFS) for control. The other part is reflected to the entrance pupil (photometric mask) and then injected into the optical fibre module. Fibred DLs convey the beams to the output module realizing the pupil densification of the interferometer. Beams are divided into two paths: a science path and a sensor path. For the second, the combined beam is divided into three spectral channels using a set of dichroics, then the three images are formed on the piston sensor detector. After the extraction of the piston error, the DL commands are then sent to coherence and/or cophase.

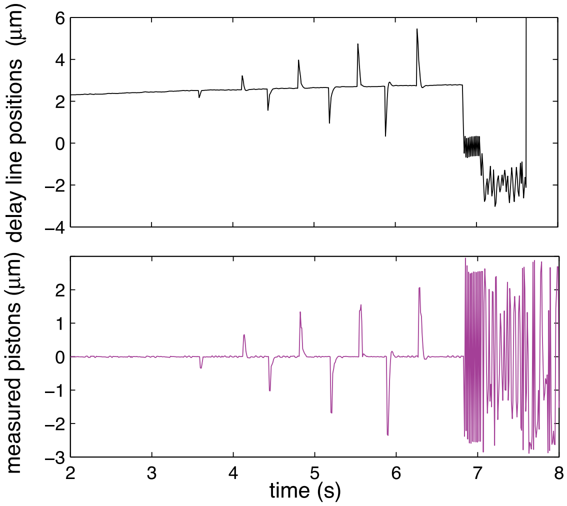

Figure 10. Determination of the CR experimentally for two spectral channels (red-green), by moving the DL and measuring the resulting piston until the limit where the algorithm diverges.

enough to track the piston and is almost the same with two or three wavelengths. However, it is clear that for atmospheric turbulence where the piston dynamic is around 5 ms, we need to improve the processing time by using a much faster computer. No limitations for this are foreseen at this time.

The second point relates to the effective CR as seen by the instrument. In fact, the value given in Section 2.1 is calculated from the manufacturing specifications of the dichroics. We have checked its value experimentally. Fig. 10 shows the pistons values we measured when moving the DL progressively in closed-loop mode. We note that the piston introduced by the DL is recovered until the limit of ±3.1 μm. This agrees with the expected value of CR for two wavelengths.

However, when using three wavelengths the algorithm diverges even when the piston is within the associated CR. This is the third issue we have encountered on the test bench and for which we propose an analysis in the next section.

Despite this issue, the result proves that we are able to extract correctly pistons up to $\pm 11(\lambda/2)$, which corresponds to a considerable achievement. In Fig. 11 we show the PSF obtained in the image plane of the sensor and the corresponding OTF modulus. The same PSF is captured in three spectral channels that we distinguish with three false colours: red for $\lambda = 665$ nm, green for $\lambda = 602$ nm and blue for $\lambda = 552$ nm. When the tracking is on, the PSF is locked in its central position, which corresponds to the maximum of contrast: all beams are thus cophased. In Fig. 12, we present the effectiveness of the tracking by plotting the flux in the central peak of the PSF as long as tracking is on. The stability is remarkable as expected with a correct cophasing of the array.

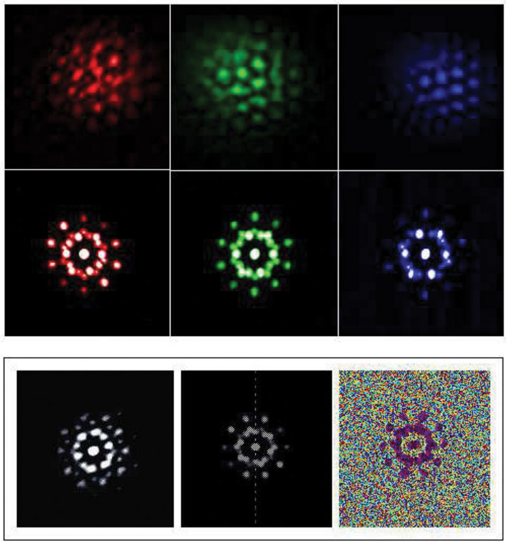

Figure 11. PSF and OTF forms in the three spectral channels, without tracking (top). In the bottom from left to right: one monochromatic PSF, the associated OTF and the phase distribution with cophasing.

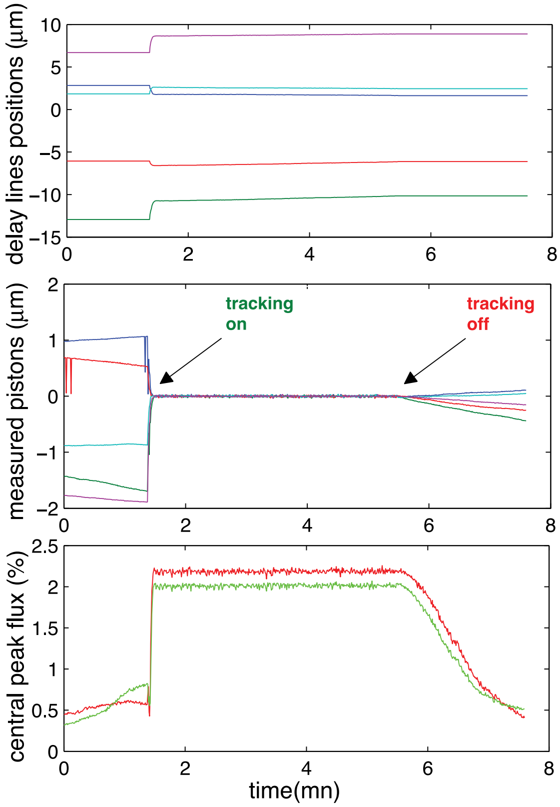

Figure 12. Position of the five DLs (top). Pistons measured on the five baselines using two channels (red-green) (middle). Flux stability in the central peak when tracking is on (bottom).

5.3 Main limitations encountered

5.3.1 Residual chromatism in the piston sensor

The optical fibres used in our experiment introduce a chromatic dispersion, which is responsible for the most limiting factor we have encountered. The chromatic dispersion has been equalized initially between the fibres but the accuracy of the method and the stability leads to residual chromatism limiting the method. For a pair of single-mode fibres, the differential chromatic dispersion comes from two effects: material dispersion and waveguide dispersion. The refractive index of the fibre is different according to the wavelength of the light, since each wavelength propagates in the fibre at a specific speed. This creates a varying delay in arrival time between the different wavelengths. Waveguide dispersion arises from the geometry of the fibre itself and the inhomogeneous refractive index between the core and the cladding. The fibres used in the SIRIUS test

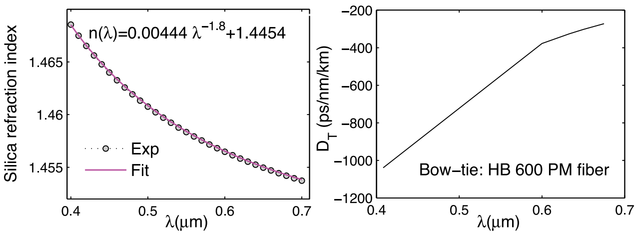

Figure 13. Refractive index of silica varies with wavelength (left). Characteristic of the chromatic dispersion in the optical fibres used in SIRIUS (right).

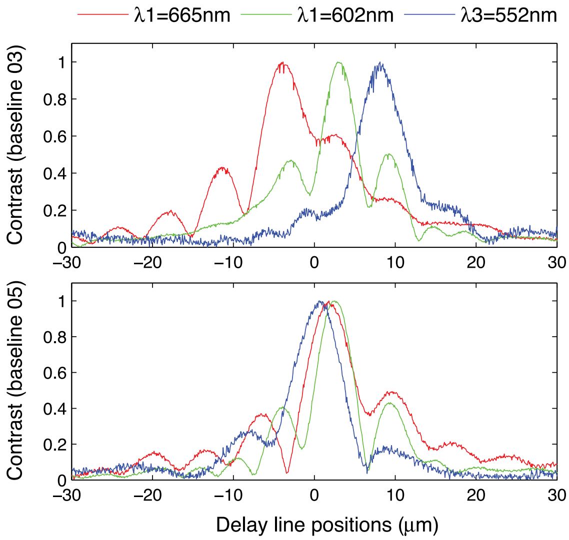

Figure 14. Contrast evolution for three spectral channels when moving the DLs along the entire excursion. Example of the strong dispersion effect on baseline 0-3 (top) and the weak effect in baseline 0-5 (bottom).

bench are of the bow-tie type with polarization-maintaining properties; their characteristic chromatic dispersion is shown in Fig. 13. It is important to note that to avoid complicating issues with the polarization, we use two polarizing filters, one before the injection into the fibres and one at the output in order to maximize the fringe contrast and cancel any variation during the fibre's manipulation. The variation of refractive index with wavelength is given by an empirical formula, which we can adjust with a power law relation. The total chromatic dispersion (D_T) is given experimentally by the manufacturer. So we can easily characterize the residual phase delay in the fibre for any wavelength.

However, the measurement of the contrast for the five baselines show a residual chromatic dispersion. This unexpected residual dispersion is obviously introduced by a non-linear effect present in some baselines. As shown in Fig. 14, baseline 0-3 is the most affected while in baseline 0-5 the effect is weak. We suppose that this effect is due to a deformation of the fibre caused by the temperature variation and the repeated contraction–relaxation of the fibre during the tracking as well as a residual of glass length equalization. This effect causes the algorithm to fail to find the correct solution when using more than two wavelengths. Therefore, it is crucial to use optical fibres with high-precision calibration.

5.3.2 Other limitations due to the fibred DLs

On the SIRIUS test bench, the fibres are used as actuators to servo control the pistons. Each one is wound around a piezo-electric drum that can contract or relax to adjust the optical length of the fibre over a stroke of about 130 µm. Thus, the wound fibres acts as DLs, and their position is controlled by the voltage applied to the piezo-electric drums. However, during our experimentation, we noted two main issues with the use of such DLs.

We found that the relation between fibre deformation and the applied voltage was not completely linear, and that the system suffers from some hysteresis. It is then difficult to determine accurately the correct DL position. This introduces a bias in the measurement of the position of the fringes in coherence mode, and, in the cophasing mode, small oscillations around the cophased position, which may cause a significant loss of contrast when using long integration times on a science camera.

A second limitation of the current fibred DLs comes from their relaxation time, which is, for large amplitude, not negligible compared to the cophasing timescale. In the current SIRIUS configuration this is not a major issue, but will become more problematic with the introduction of the piston generator device on the SIRIUS test bench.

6 PERFORMANCE WITH OPTICAL TURBULENCE

In this section, we show the result of an experiment we realized on the SIRIUS bench to check the performance of the method with optical turbulence. We designed a mask introducing random piston perturbations into the individual incoming beams. This creates, as for real observations, random fluctuations of the piston. The perturbation created by the mask was set to the one measured at the VLT site (Paranal).

6.1 Introducing a piston generator to the SIRIUS test bench

A piston generator was mounted on the SIRIUS bench next to the photometric mask as shown in Fig. 15. The mask consists of a silica disk into which encoded bi-dimensional aberrations have been introduced (Mourard et al. 2012). The beams pass through the aberration zone except for the central beam, which we choose as the piston reference. The central beam is thus not perturbed and its optical axis corresponds to the mask's rotation axis. A stepper motor is used to control the rotation frequency, which is set to correspond to the real turbulence dynamic as measured at Paranal (Dali Ali et al. 2010).

6.2 Results and discussion

Using the mask, a series of tests were performed to compare the piston obtained with our method and the known values generated by the mask. In Fig. 16 we plot, for one baseline (0-4), the contrast and the corresponding piston given by the algorithm in open-loop mode. We note that the piston is correctly recovered as soon as the contrast is above a certain value. Therefore, we add this condition to the contrast value in the algorithm to validate the pistons that have been determined. This avoids, as shown in Fig. 16, systematic jumps (magenta curve) of the piston value and significantly improves the follow-up of the piston (black curve). The repeatability of the solution matches the periodic rotation of the mask. This shows the accuracy of the method and the stability in the solution determination.

Finally, we compare in Fig. 17 the output profile of pistons determined by the algorithm and the profile we draw on the phase masks.

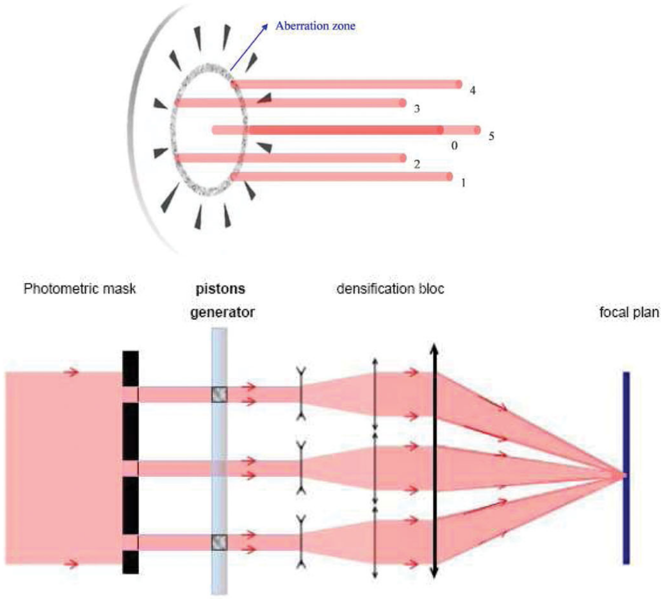

Figure 15. Design of the piston mask (above). Configuration of the mask on the SIRIUS bench (bottom).

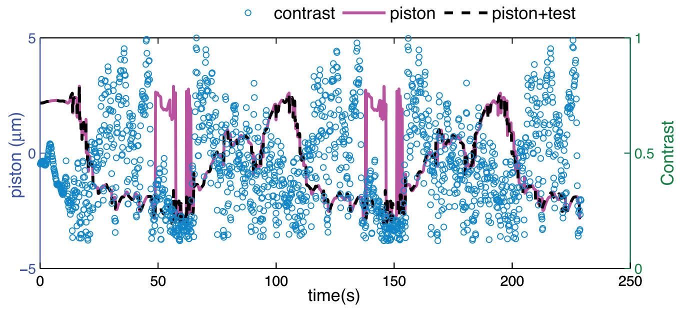

Figure 16. Measured pistons (magenta curve) with the corresponding contrast (blue circles) for baseline 0-4. By adding a condition to the contrast value, we avoid jumps of the piston value (black-dashed curve).

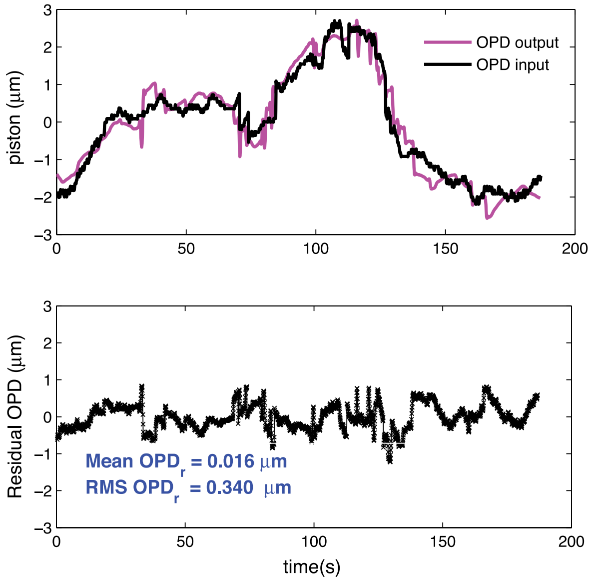

Figure 17. Top: For one complete tour of the mask, the measured piston (magenta curve) fits well the profile introduced by the mask (black line). Bottom: Residual OPDs. For this example, the mean value of the residual OPDs is 0.016 µm with RMS = 0.34 µm.

The difference between them is given by the residual OPD. The average value of this last remains low (0.016 µm) with 0.34 µm RMS. So the agreement between the two profiles is good.

The results obtained during the final experiment with the presence of turbulence are very encouraging although we did not succeed in correctly applying the full three-colour algorithm because of the residual chromatism in some fibres. The choice to use fibres was made initially with the prospect of developing a prototype of a future space experiment. Taking advantages of spatial filtering for optimized performance is of course mandatory but this could be done, in principle, without fibres. In any case, the flexibility brought by the fibres in the optical set-up is also a great advantage that has to be considered. As a clear lesson learned during this experiment, one can say that the calibration of the chromatism in the fibres is a complex task and keeping it stable over a long period of time is difficult. This was certainly the main limitation we encounter in this project.

7 THE CPD METHOD AMONG THE GROUP AND PHASE DELAY PRINCIPLES

In this section we compare the CPD implementation with the other existing methods used for fringe sensing, as presented in Table 3. Advantages and limitations are compared in Table 4.

Table 3. Concepts applied for fringe sensing.

Method	Work	Application
ABCD	Colavita et al. (1998)	NPOI-PTI-Keck CHARA-VLTI
FS	Gai et al. (2004)	VLTI(FINITO)/IOTA
DF	Koechlin et al. (1996)	GI2T-SUSI
DS	Borkowski et al. (2005)	–
CPD	Tarmoul et al. (2010b)	SIRIUS

Table 4. Comparison of the main characteristics of fringe sensing systems.

Method	Configuration	N_T	N_{pixel}	CR
ABCD	1D	2	4	Ł$_c$
DF	1D	2	↑ with $\Delta\lambda$, $n\lambda$	L_c
DS	2D	N_T large	↑ with $n\lambda$	L_c
CPD	2D	N_T large	$(90 \times 90) \times 3$	L_c

Up to now, the classical method for fine cophasing is ABCD combined with additional dispersion to allow wide coherence. Group delay traditionally uses spectral dispersion. So, the difference between these methods lies in the optical set-up and the type of data processing. For example, different implementations of DF use different methods of piston estimation: Fourier transform methods (fringe peaks) as in DS or in CPD, or fringe model fitting for an increased gain in stability (Colavita 1999; Mozurkewich & Traore 2010).

The number of pixels needed for the DF method increases with the number of channels ($n\lambda$) and/or with the spectral width ($\Delta\lambda$). This is avoided with our CPD method, where the number of spectral bands is not larger than three. Indeed, a piston sensor using many beams consumes fewer pixels with the 2D pupil arrangement and with few multi-chromatic images than with the classical one-dimensional (1D) pupil arrangement and DF. Consequently, it is less time-consuming and more sensitive, so that it will improve both the accuracy and the sensitivity.

As said previously, the entrance pupil of the piston sensor is rearranged in a non-redundant pupil configuration with concentric circles to feed the piston sensor with the most compact chromatic images (Patru et al. 2009). Indeed, using concentric rings allow a non-redundant configuration with the smallest minimum baseline. This corresponds to the smallest direct imaging field of view (DIF) diameter, which is equal to DIF $=\lambda/(B_{\mathrm{min}}(\gamma - 1))$ in units of radians, with γ the densification factor (Lardière et al. 2007). Consequently, a pupil composed of concentric rings provides the smallest number of requested pixels on the CCD.

The number of pixels depends on the number of spectral channels and the size of the densified image, which is a function of the CCD sampling and of the DIF diameter. This can be written as:

$$N\ [\mathrm{pixel}] = (\mathrm{DIF}\ [\mathrm{pixel}])^2\, n\lambda, \tag{14}$$

which can be written as:

$$N\ [\mathrm{pixel}] = \left(\frac{\mathrm{DIF}\ [\mathrm{rad}]}{\mathrm{Resel}\ [\mathrm{rad}]} \mathrm{Resel}\ [\mathrm{pixel}]\right)^2 n\lambda. \tag{15}$$

The resolution element Resel $=\lambda/B_{\mathrm{max}}$ in unit of radians. Each resolution element is sampled on n_S pixels, where $n_S =$ Resel [pixel] is the sampling rate on the CCD, which equals here 6 pixels per resel. Thus, we can write:

$$N\ [\mathrm{pixel}] = \left(\frac{\lambda/((\gamma - 1)B_{\mathrm{min}})}{\lambda/B_{\mathrm{max}}} n_S\right)^2 n\lambda. \tag{16}$$

The partial densification of a factor 0.4 enlarges the number of pixels, but it is imposed by the Nyquist theorem to avoid overlapping of the Fourier peaks. Knowing that the maximal densification factor is $\gamma_{\mathrm{max}} = B_{\mathrm{min}}/d_i = \gamma/0.4 = 2.5\gamma$, then:

$$N\ [\mathrm{pixel}] = \left(\frac{B_{\mathrm{max}}}{B_{\mathrm{min}}} \frac{n_S}{(0.4 B_{\mathrm{min}}/d_i - 1)}\right)^2 n\lambda. \tag{17}$$

For the configuration with a concentric ring, the number of telescopes may be approximated by $N_T \approx (B_{\mathrm{max}}/B_{\mathrm{min}})^2$ (Patru et al. 2009):

$$N\ [\mathrm{pixel}] = N_T \left(\frac{n_S}{(0.4 B_{\mathrm{min}}/d_i - 1)}\right)^2 n\lambda, \tag{18}$$

or

$$N\ [\mathrm{pixel}] = N_T \left(\frac{n_S}{(\gamma - 1)}\right)^2 n\lambda. \tag{19}$$

So, according to Labeyrie (1996), Lardière et al. (2007) and Patru et al. (2009), we can say that the use of pixels is optimum, by concentrating all the flux into the densified image.

For the SIRIUS implementation, we need in principle $(3 \times 15)^2 \times 3 = 6075$ pixels corresponding to an implementation of three images of 45×45 pixels. Our current setting is 90×90 with an oversampling factor of 2. For a 100-beam piston sensor, which corresponds to DIF $\approx$12 resels (Patru et al. 2009), we will only need $(12 \times 15)^2 \times 3 \simeq 10^5$ pixels, i.e. three images of typically 180×180 pixels. This can be compared with the 1500×2200 CCD requested in Mozurkewich & Traore (2010) with an important improvement of more than a factor 20.

Taking into account all these aspects, we can see that the CPD method is well adapted to the 2D pupil configuration or when the number of telescopes (N_T) increases and thus the pairwise recombination becomes complex and inappropriate. SNR comparisons are very difficult to do as the different implementations vary considerably in terms of spectral bands, detectors and number of beams. To avoid confusion. we did not present here such computations.

8 CONCLUSION

One of the main constraints of future interferometers is the recombination of the input beams within a fraction of a wavelength to reach the theoretical performance. Considering the large number of apertures of the future arrays, developing an efficient and easy-to-implement cophasing system is thus of utmost importance. Robustness is also mandatory for good quality observations and an efficient use of the night time.

In this paper, we have presented a new approach to deal with the group and phase delays with spectral dispersion. We have demonstrated that our original implementation correctly meets the main specifications of cophasing, in terms of CR up to $\pm 11\lambda/2$ and with a possible resolution of the piston of the order of $\lambda/30$. The phase retrieval method uses three filtered images recorded simultaneously and processed in real time.

A CPD sensor has been implemented on the SIRIUS test bench (Tarmoul et al. 2010b) at Observatoire de la Côte d'Azur, Grasse, France. It benefits considerably from the hypertelescope recombining scheme with a multi-axial combiner and a pupil densifier. It allows simplification of an optical scheme with a large number of sub-pupils. It helps to optimize the signal on the detector, by minimizing the number of pixels and by maximizing the flux per pixel and the sensitivity of the system. The method also benefits from the single-mode fibres used to rearrange the array configuration into a partially densified pupil and to cophase the beams by stretching the fibres. Single-mode spatial filtering improves the accuracy of the estimated residual pistons and reduces the phase jump effects.

Apart from a few resolvable technical problems due to the actual implementation (residual differential chromatism between fibres), the results obtained on the SIRIUS test bench show the ability of our proposed method to retrieve piston errors over an extended range of the OPD and to cophase the beams up to a fraction of the wavelength. The CPD method has been proved to be robust and to use large spectral bands correctly, which is mandatory for an astronomical implementation and faint magnitude goals.

ACKNOWLEDGEMENTS

This project has benefited from European funds under the FP7-OPTICON project, contract number 226604.

REFERENCES

Borkowski V., Labeyrie A., Martinache F., Peterson D., 2005, A&A, 429, 747
Buscher D. F., Young J. S., Baron F., Haniff C. A., 2008, SPIE Conf. Series, 7013, 1,
Colavita M. M., 1999, PASP, 111, 111
Colavita M. M. et al., 1998, SPIE Conf. Series, 3350, 776
Dali Ali W. et al., 2010, A&A, 524, A73
Gai M. et al., 2004, SPIE Conf. Series, 5491, 528
Glindemann A. et al., 2004, SPIE Conf. Series, 5491, 447
Gonsalves R. A., 1982, Opt. Eng., 21, 829
Houairi K., Cassaing F., 2009, J. Opt. Soc. America A, 26, 2503
Koechlin L. et al., 1996, Applied Opt., 35, 3002
Labeyrie A., 1996, A&AS, 118, 517
Lardière O., Martinache F., Patru F., 2007, MNRAS, 375, 977
Lebouquin, 2012, ESO internal report
Lebouquin, 2012, ESO internal report
Lofdahl M. G., Eriksson H., 2001, Opt. Eng., 40, 984
Martinache F., 2004, J. Opt. A, 6, 216
Monnier J. D. et al., 2008, SPIE Conf. Series, 7013, 1
Morel S., Traub W. A., Bregman J. D., Mah R. W., Wilson E., 2000, SPIE Conf. Series, 4006, 506
Mourard D. et al., 2012, SPIE Conf. Series, 8445, 1
Mozurkewich D., Traore A., 2010, SPIE Conf. Series, 7734, 1
Patru F., Mourard D., Lardière O., Lagarde S., 2007, MNRAS, 376, 1047
Patru F. et al., 2008, A&A, 477, 345
Patru F., Tarmoul N., Mourard D., Lardière O., 2009, MNRAS, 395, 2363
Patru F., Chiavassa A., Mourard D., Tarmoul N., 2010, SPIE Conf. Series, 7734, 1
Shao M. et al., 1988, A&A, 193, 357
Tarmoul N., Mourard D., Hénault F., 2008, SPIE Conf. Series, 7013, 1
Tarmoul N. et al., 2010, SPIE Conf. Series, 7734, 1
Tarmoul N., Hénault F., Mourard D., Le Bouquin J.-B., Jocou L., Kern P., Berger J.-P., Absil O., 2010, SPIE Conf. Series, 7734, 1
ten Brummelaar T. A. et al., 2005, ApJ, 628, 453

This paper has been typeset from a TEX/LATEX file prepared by the author.